

Receptivity of a supersonic jet due to acoustic excitations near the nozzle lip

Binhong Li¹, Sicheng Zhang¹ and Benshuai Lyu^{1,2†}

¹State Key Laboratory of Turbulence and Complex Systems, College of Engineering, Peking University, 5 Yiheyuan Road, Haidian District, Beijing 100871, China

²Laoshan Laboratory, Qingdao 266100, PR China

(Received xx; revised xx; accepted xx)

In this paper, we develop an analytical model to investigate the generation of instability waves triggered by the upstream acoustic forcing near the nozzle lip of a supersonic jet. This represents an important stage, i.e. the jet receptivity, of the screech feedback loop. The upstream acoustic forcing, resulting from the shock-instability interaction, reaches the nozzle lip and excites new shear-layer instability waves. To obtain the newly-excited instability wave, we first determine the scattered sound field due to the upstream forcing using the Wiener-Hopf technique, with the kernel function factored using asymptotic expansions and overlapping approximations. Subsequently, the unsteady Kutta condition is imposed at the nozzle lip, enabling the derivation of the dispersion relation for the newly-excited instability wave. A linear transfer function between the upstream forcing and the newly-excited instability wave is obtained. We calculate the amplitude and phase delay in this receptivity process and examine their variations against the frequency. The phase delay enables us to re-evaluate the phase condition for jet screech and propose a new frequency prediction model. The new model shows improved agreement between the predicted screech frequencies and the experimental data compared to classical models. It is hoped that this model may help in developing a full screech model.

1. Introduction

Screech is a phenomenon characterized by discrete acoustic tones in imperfectly expanded supersonic jet flows (Raman 1999; Edgington-Mitchell 2019). Its high intensity can lead to sonic fatigue and severe damage to aircraft structures, emphasizing the importance of understanding its underlying mechanism. In the pioneering work by Powell (1953*a*), he proposed the well-known feedback-loop mechanism consisting of four stages: the downstream propagation of instability waves, the interaction between shock and instability waves, the upstream propagation of acoustic waves, and the jet receptivity at the nozzle lip. Powell further introduced the gain and phase conditions necessary for

† Email address for correspondence: b.lyu@pku.edu.cn

establishing the screech. These two conditions laid the foundation of following jet screech research.

The screech frequency, herein defined as f , has gained much attention in early research. Powell suggested that it can be calculated by assuming constructive interference at 180° between shock-cell sources, i.e.

$$f = \frac{U_c}{s(1 + M_c)}, \quad (1.1)$$

where s , U_c , and M_c are the shock cell spacing, the convection velocity, and the convective Mach number of the instability waves, respectively. Note, strictly speaking, (1.1) is not a traditional phase condition in the sense that the overall phase change during the four stages of screech is assumed to be $2N\pi$, where N is an integer. Nonetheless, the predicted results using (1.1) demonstrated satisfactory agreement with experimental data regarding rectangular nozzles. Subsequently, Tam *et al.* (1986) proposed the weakest link theory, suggesting screech as the limit of broadband shock-associated noise (BBSAN) when the observer angle approaches 180° . Based on these two models, new frequency prediction formulas were developed to include effects of nozzle geometry, including rectangular nozzles with different aspect ratios (Tam 1986; Tam & Reddy 1996), bevelled rectangular nozzles (Tam *et al.* 1997), and elliptic nozzle (Tam 1988). These model predictions exhibited favourable agreement with experimental data.

However, in round jets, Powell observed sudden changes in the screech frequency with increasing inlet pressure, a phenomenon termed mode staging. Powell categorized these changes into four distinct modes: A, B, C, and D, with mode A further divided into modes A1 and A2 (Merle 1956). It is evident that the aforementioned formulas, which showed continuous frequency predictions against the nozzle inlet pressure, proved inadequate in predicting mode staging. The physical mechanism of mode staging necessitated further investigation.

To investigate the mode staging phenomenon, Li & Gao (2010) introduced the phase condition as an alternative to the constructive interference condition to predict the screech frequency. They conducted comprehensive numerical simulations to thoroughly investigate various parameters regarding the phase condition, including the convection velocity of instability waves, the effective sound source region, and the shock spacing. Their simulation results demonstrated agreement with experimental data when the cycle numbers contained in the feedback loop were changed, suggesting that the phase condition might provide insights into the underlying mechanism of the mode staging phenomenon. Recent years have witnessed a re-evaluation of the phase condition, see for example Jordan *et al.* (2018) and Mancinelli *et al.* (2021). These new theories emphasized the crucial role played by the guided-jet mode in completing the feedback loop of jet screech, as evidenced by recent publications (Gojon *et al.* 2018; Edgington-Mitchell *et al.* 2018; Li *et al.* 2020). According to these studies, both the A1 and A2 modes were closed by guided-jet modes rather than free acoustic waves. Moreover, the guided-jet mode was

found to be active in all screech modes (Edgington-Mitchell *et al.* 2022), and its excitation can be attributed to interactions between the instability waves and the optimal order as well as suboptimal wavenumber components of the shock structures (Nogueira *et al.* 2022; Edgington-Mitchell *et al.* 2022; Li *et al.* 2023). The guided-jet mode due to the interaction between instability waves and the suboptimals is shown to be responsible for closing the feedback loop in multiple stages of jet screech. The role of guided-jet modes was also examined under the circumstances of screeching twin jets (Stavropoulos *et al.* 2023), which showed similar trends to those observed in single jets.

To invoke the phase condition to predict the mode staging phenomenon, an important step is to determine the phase delay between the upstream forcing and the newly-triggered instability waves. This necessitates a close examination of the receptivity process of the jet screech. Previous investigations conducted relevant research using experimental measurements, numerical simulations, and analytical models.

Early research primarily focused on experimental measurements, which revealed that modifications to the nozzle lip, such as nozzle thickening, could change both the mode and amplitude of screech tones (Norum 1983; Ponton & Seiner 1992; Raman 1997). Additionally, an acoustic reflector placed upstream or downstream of the nozzle lip was shown to significantly impact screech amplitude (Nagel *et al.* 1983; Norum 1984; Raman *et al.* 1997). Moreover, it was found that installing conical reflector surfaces around a round nozzle exit could cause significant changes in the mode staging behaviour (Morata & Papamoschou 2023). Recently, Alapati & Srinivasan (2024) showed that when the surface roughness of the nozzle lip increases, the screech amplitude decreased or even disappeared. These observations underscored the key role played by the jet receptivity in determining the screech amplitude and frequencies.

Besides experimental measurements, several numerical simulations were conducted to investigate jet receptivity. Shen & Tam (2000) explored the effects of nozzle-lip thickness on the intensities of the axisymmetric screech tones. They found that at low supersonic Mach numbers, the changes of the screech amplitude were not significant with a thickened nozzle lip, which aligned with experimental observations (Ponton & Seiner 1992). Recent years have seen an increase in research on jet receptivity. Karami *et al.* (2020) defined a transfer function at the nozzle lip between the external disturbance and the initial conditions of the vortical instability in the case of impinging jets. Their findings indicated that the scattering efficiency was related to the nondimensionalized frequency, the azimuthal wavenumber, and the pulse location. Subsequently, Karami & Soria (2021) incorporated the effects of nozzle geometry into their analysis. They noted that an infinite-lipped nozzle supported higher amplitude upstream-propagating waves both inside and outside the jet flow compared to the thin nozzles. Boegy (2022) conducted Large Eddy Simulations (LES) to explore the interaction between upstream-propagating guided jet modes and shear-layer instability waves near the jet nozzle. He observed that the frequency of the most amplified Kelvin-Helmholtz instability wave fell within the

narrow frequency bands of the guided-jet mode. The effects of the nozzle thickness were also investigated in Bogey (2023), where it was found that a thickened nozzle lip led to an increase in the near-field sound pressure level downstream of the jet nozzle.

Despite numerous experimental and numerical investigations, not many analytical models were developed to model the jet receptivity. Tam (1978) investigated the excitation of instability waves in infinitely-long two-dimensional free shear layer by acoustic waves, which was solved by using the Green's function of the problem. He found that to excite instability waves at moderate subsonic flow Mach numbers, an acoustic beam inclined at an angle of 50° to 80° to the shear flow is the most effective. Another notable study conducted by Kerschen (1996) examined the jet receptivity due to acoustic excitations and introduced a receptivity coefficient to predict the screech amplitude. However, comprehensive details of this model appeared missing in the open literature. Another study by Barone & Lele (2005) employed a combined theoretical and computational approach and revealed that upstream-propagating acoustic perturbations could excite instability waves in the jet mixing layer. They further observed that the thickness of the nozzle lip significantly influenced the receptivity process, which accorded with numerous experimental observations.

In spite of numerous studies on jet receptivity, the phase delay in the receptivity process remains unclear. Previous studies often assumed a fixed phase delay such as 0 or $\pi/4$ (Jordan *et al.* 2018; Mancinelli *et al.* 2021; Stavropoulos *et al.* 2023; Li *et al.* 2023). To obtain the correct phase delay, instead of relying on assumed values, an analytical model of the jet receptivity is needed. More specifically, a linear transfer function between the upstream forcing and the newly-generated instability wave is desired. Therefore, the primary objective of this paper is to develop such a model to improve our understanding of jet receptivity.

This paper is structured as follows: section 2 provides a detailed analytical derivation of the model, including the formulation of the Wiener-Hopf problem, the decomposition of the kernel function, and the determination of the dispersion relation. A linear transfer function between the upstream forcing and the newly-excited instability waves is obtained. In section 3, we present our results based on the derived transfer function, where a new formula is proposed to predict the screech frequency. Finally, section 4 concludes this paper.

2. Analytical formulation

2.1. The Wiener-Hopf equation

Inspired by Crighton (1992), who investigated jet-edge tones, we focus on a two-dimensional jet flow of a vortex-sheet type in this paper. To render the model more realistic, the incident acoustic wave takes an asymptotic form generated through the

interaction between shock and instability waves, as obtained previously by the authors (Li & Lyu 2022, 2023).

Schematic illustration is shown in figure 1. As we can see, a supersonic jet is issued from the nozzle and takes the form of a vortex sheet. The coordinate axes (x, y) are chosen to be parallel and perpendicular to the nozzle centreline, respectively, while the origin point O is located at the center of the nozzle exit plane. According to Pack (1950), the base flow is chosen as the fully expanded jet velocity \tilde{U} , which is different from the jet exit velocity \tilde{U}_j . \tilde{D} is the height of the fully expanded jet. Note that \tilde{D} is generally not equal to the height of the nozzle \tilde{D}_0 (Tam 1972), but is less or greater than \tilde{D}_0 depending on whether the jet is underexpanded or overexpanded (Tam & Tanna 1982). The densities inside and outside the jet are denoted by $\tilde{\rho}_i$ and $\tilde{\rho}_o$, respectively, while $\tilde{T}_{0,i}$ and \tilde{T}_o represent the total reservoir temperature and the ambient temperature outside the jet, respectively. The nozzle lips, represented by two flat plates in figure 1, are assumed to be semi-infinite with a negligible thickness, extending to $-\infty$ in the x direction. Downstream of the nozzle lip, an acoustic wave, with a speed of sound \tilde{a}_∞ and a frequency of $\tilde{\omega}$, is emitted from a source region and propagates upstream to the nozzle lip, triggering the instability waves.

To simplify the problem, we nondimensionalize velocities and lengths by \tilde{U} and \tilde{D} , respectively. In addition, densities and temperatures are nondimensionalized by $\tilde{\rho}_o$ and \tilde{T}_o , respectively. Note that we use the symbols with a tilde to represent dimensional variables, while those without denote non-dimensional variables. For example, after the nondimensionalization, the jet exit velocity is U_j and the base flow takes the form

$$\mathbf{u}_0 = \begin{cases} 0, & |y| > 1/2, \\ \mathbf{e}_x, & |y| \leq 1/2, \end{cases} \quad (2.1)$$

where \mathbf{e}_x is the unit vector in the x direction.

Considering that the mean pressure outside and inside of the vortex sheet remains the same when a perfect gas is assumed, the density ratio between the outside and inside of the vortex sheet, here defined as σ , is equal to M_o^2/M_i^2 . Here, M_o and M_i are defined as $1/c_o$ and $1/c_i$, respectively, where c_o and c_i represent the nondimensional speed of sound outside and inside of the jet, respectively. The relation between the two Mach numbers is determined using Crocco-Busemann's rule, i.e.

$$M_o = \frac{M_i}{\sqrt{1 + \frac{\gamma-1}{2} M_i^2}} \nu^{1/2}, \quad (2.2)$$

where ν denotes the temperature ratio between $\tilde{T}_{0,i}$ and \tilde{T}_o , and γ represents the specific heat ratio.

Before proceeding to solve the problem, it is useful to examine the designed transfer function using the Buckingham π theorem. As mentioned above, eight physical variables are involved in this model, i.e. \tilde{D} , \tilde{U} , $\tilde{\rho}_i$, $\tilde{\rho}_o$, $\tilde{T}_{0,i}$, \tilde{T}_o , \tilde{a}_∞ , and the frequency of the acoustic wave $\tilde{\omega}$, while four independent dimensions can be found. Employing the Buckingham π

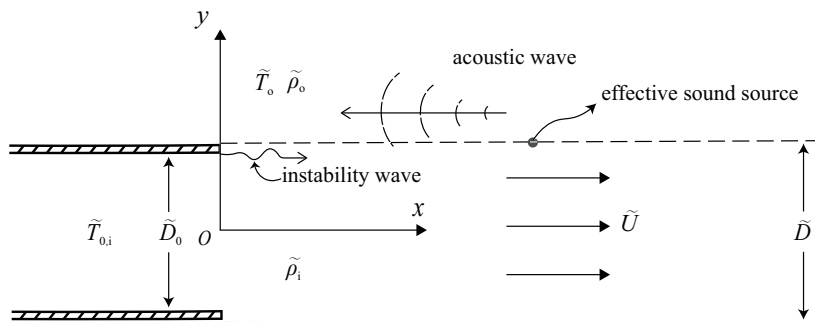


FIGURE 1. The schematic of the vortex-sheet flow configuration and Cartesian coordinates. The origin is fixed at the centre of the nozzle while x - and y - axes represent the streamwise and cross-flow coordinates, respectively.

theorem, it is evident that the transfer function H between the newly-excited instability wave and the acoustic waves is related to four nondimensional parameters. These four parameters are chosen to be the Mach number M_i , the Strouhal number ω , the temperature ratio ν , and the density ratio σ . The density ratio can be calculated using ν and M_i through the Crocco-Busemann's rule (2.2). Therefore, there remain three independent nondimensional parameters and our objective is to find the transfer function $H(M_i, \omega, \nu)$ in the subsequent analysis.

To have a realistic incident acoustic wave, we take the result obtained in the shock-instability interaction work (Li & Lyu 2022, 2023). Pack's model was used to describe shock waves, while instability waves were calculated using the linear stability analysis. The resulting nondimensionalized velocity potential function of the acoustic waves due to one-cell interaction can be obtained by performing the inverse Fourier transform, i.e.

$$\phi_{\text{in}}(x, y) = \frac{1}{2\pi} \int_{-\infty}^{\infty} D_o(\lambda) \exp(-i\lambda x + \sqrt{\lambda^2 - \omega^2 M_o^2} y) d\lambda. \quad (2.3)$$

Herein λ denotes the streamwise wavenumber and $D_o(\lambda)$ represents a coefficient, which can be readily calculated when M_o and ω are provided. The detailed expression of $D_o(\lambda)$ can be found in Li & Lyu (2023). The integration in (2.3) can be estimated (in the far field) by the saddle point method. The closed-form asymptotic potential function can be expressed as follows

$$\phi_{\text{in}}(r, \theta) = \sqrt{\frac{\omega M_o}{2\pi}} \frac{e^{i\omega(M_o r - t - \pi/4)}}{\sqrt{r}} D_o(-\omega M_o \cos\theta) \sin\theta, \quad (2.4)$$

where θ is the observer angle with respect to the downstream direction and r represents the distance from the screech source region to the nozzle lip.

As shown in (2.4), $\phi_{\text{in}}(r, \theta)$ depends on r . Experimental observations indicated that the screech source was situated several shock cells downstream from the nozzle exit (Suda *et al.* 1993; Kaji & Nishijima 1996; Malla & Gutmark 2017). Therefore, the streamwise

distance between the source position to the nozzle lip is written as

$$h = ns, \quad (2.5)$$

where n typically takes the value of 3, 4, or 5 (Suda *et al.* 1993; Li & Gao 2010; Malla & Gutmark 2017), and s denotes the shock spacing, which can be calculated using Pack's model (Pack 1950; Tam 1986).

We consider the potential function of the upstream forcing $\Phi_{\text{in}}(r, \theta)$ in the proximity of the nozzle lip, where the value of $y - 1/2$ is relatively small compared to $|x| = h$. Therefore, the distance r in (2.4) can be approximated as $r \approx h$. Similarly, we have $\sin \theta \approx (y - 1/2)/h$ and $\cos \theta \approx 1$. Consequently, in the vicinity of the nozzle, the potential function Φ_{in} can be reformulated to a similar form to that in Crighton (1992), i.e.

$$\Phi_{\text{in}}(Y) = GY, \quad (2.6)$$

where

$$G = \sqrt{\frac{\omega M_o}{2\pi h^3}} D_o(\omega M_o) e^{i\omega(M_o h - \pi/4)}, \quad (2.7)$$

$$Y = y - \frac{1}{2}. \quad (2.8)$$

The goal is therefore to find the response of the jet flow due to the upstream forcing GY near the nozzle lip. In this paper, we focus on the upper half-plane ($y > 0$), while a similar analysis can be carried out for the lower half-plane. Considering that the time-harmonic assumption is used, the factor $e^{-i\omega t}$ in all the time-dependent fields is omitted for clarity in the rest of this paper. Because we assume the initial base flow to be irrotational and inviscid both inside and outside of the vortex sheet (Batchelor & Gill 1962), the velocity potential induced by the incident acoustic wave near the nozzle lip can be described by a potential function. Therefore, taking into account (2.6), the total velocity potentials outside and inside the jet flow can be defined by

$$\Phi = GY + \phi(x, y), \quad (2.9)$$

$$\Psi = GY + \psi(x, y), \quad (2.10)$$

respectively, where ϕ and ψ are the corresponding potential functions of the scattered sound fields in the region $y > 1/2$ and $0 \leq y \leq 1/2$, respectively.

It is known that ϕ and ψ both satisfy the convective wave equation, i.e.

$$\nabla^2 \phi + \omega^2 M_o^2 \phi = 0, \quad (2.11)$$

$$\nabla^2 \psi + \left(\omega + iM_1 \frac{\partial}{\partial x} \right)^2 \psi = 0. \quad (2.12)$$

Hard-wall conditions are imposed on $y = 1/2$ for $-\infty < x \leq 0$. Note that, strictly speaking, these conditions should be applied at $y = \tilde{D}_0/2\tilde{D}$, which can be either less than or greater than $1/2$ depending on whether the jet is underexpanded or overexpanded (Tam

& Tanna 1982). However, as mentioned earlier, the difference between $\tilde{D}_0/2\tilde{D}$ and $1/2$ is relatively small compared to the distance r . To enable analysis progress, we neglect this difference and assume that the plate is nearly parallel to the boundary of the jet. Therefore, we obtain

$$\frac{\partial\phi}{\partial y} = \frac{\partial\psi}{\partial y} = -G \quad (y = 1/2, -\infty < x \leq 0). \quad (2.13)$$

The absence of decay in the forcing term $-G$ leads to convergence issues when the Fourier transform is applied to (2.13). To circumvent this problem, Crighton (1992) replaced (2.13) by

$$\frac{\partial\phi}{\partial y} = \frac{\partial\psi}{\partial y} = -Ge^{\epsilon x}, \quad (2.14)$$

where ϵ is a real and positive term, which retains the physical characteristics of the upstream forcing near the nozzle lip but removes the forcing further upstream. We follow the same treatment here.

The kinematic and dynamic boundary conditions can be used on the vortex sheet at $y = 1/2, 0 < x < \infty$, i.e.

$$\left(-i\omega + \frac{\partial}{\partial x}\right) \frac{\partial\phi}{\partial y} = -i\omega \frac{\partial\psi}{\partial y}, \quad (2.15)$$

$$-i\omega\sigma\phi = \left(-i\omega + \frac{\partial}{\partial x}\right) \psi. \quad (2.16)$$

Fourier transforms $\phi(k, y), \psi(k, y)$ are defined by

$$\phi(k, y) = \int_{-\infty}^{+\infty} \phi(x, y) e^{ikx} dx, \quad (2.17)$$

$$\psi(k, y) = \int_{-\infty}^{+\infty} \psi(x, y) e^{ikx} dx, \quad (2.18)$$

where k is the wavenumber in the streamwise direction. Multiplying (2.11) and (2.12) with e^{ikx} and subsequently integrating both expressions with respect to the variable x , solutions to (2.11) and (2.12) can be found upon invoking the far-field boundary condition, i.e.

$$\phi(k, y) = \phi^*(k) e^{-\gamma_1(k)y}, \quad (2.19)$$

$$\psi(k, y) = \psi_s^*(k) \sinh \gamma_2(k)y + \psi_c^*(k) \cosh \gamma_2(k)y, \quad (2.20)$$

where

$$\gamma_2(k) = \sqrt{k^2 - (\omega + k)^2 M_1^2} \quad \text{and} \quad \gamma_1(k) = \sqrt{k^2 - \omega^2 M_0^2}. \quad (2.21)$$

Herein, $\phi^*(k)$, $\psi_s^*(k)$, and $\psi_c^*(k)$ are functions of k , whose detailed forms will be specified subsequently. To satisfy the far-field condition, the real part of γ_1 should be positive, and its branch cut will be specified later. It is well-known that both symmetric (varicose) and antisymmetric (sinuous) instability modes can exist inside the jet. But for jet flows from high-aspect-ratio rectangular nozzles, the sinuous mode is dominant (Edgington-Mitchell 2019). Therefore, we consider the antisymmetric mode in this study, while the symmetric

mode can be examined in a similar way should interest arise. In this case, $\psi(k, y)$ reduces to

$$\psi(k, y) = \psi_s^*(k) \sinh \gamma_2(k) y. \quad (2.22)$$

In what follows, we use the Wiener-Hopf method to solve this boundary-value problem specified by (2.19), (2.22) and boundary conditions (2.14), (2.15), and (2.16). Using (2.14), we can obtain

$$\phi'(k, 1/2) = \phi'_+(k, 1/2) + \frac{iG}{k - i\epsilon}, \quad (2.23)$$

where the prime represents the first derivative with respect to y and $\phi_+(k, 1/2)$ is defined by

$$\phi_+(k, 1/2) = \int_0^\infty \phi(x, 1/2) e^{ikx} dx. \quad (2.24)$$

Considering the kinematic boundary condition across the vortex sheet, i.e. (2.15), and the boundary conditions imposed on the nozzle lip, i.e. (2.14), we have

$$(k - i\epsilon) \psi_s^*(k) \cosh \gamma_2(k)/2 - \frac{G}{\omega} \epsilon = - \left(1 + \frac{k}{\omega}\right) (k - i\epsilon) \frac{\gamma_1(k)}{\gamma_2(k)} \phi^*(k) e^{-\gamma_1(k)/2}. \quad (2.25)$$

Following Crighton (1992), the term $\frac{G}{\omega} \epsilon$ on the left-hand side of (2.25) is omitted, considering that ϵ is a small term.

Now we define a new function related to the difference between the pressures outside and inside the vortex sheet as $D(k, 1/2)$, i.e.

$$D(k, 1/2) = \int_{-\infty}^\infty \left(-i\omega\sigma\phi(x, 1/2) - \left(-i\omega + \frac{\partial}{\partial x} \right) \psi(x, 1/2) \right) e^{ikx} dx. \quad (2.26)$$

Due to the continuity of the pressure across the vortex sheet, i.e. (2.16), the pressure difference vanishes when $x > 0$. Therefore, $D(k, 1/2)$ reduces to

$$D(k, 1/2) = -i\omega\sigma\phi_-(k, 1/2) - (-i\omega - ik)\psi_-(k, 1/2) + \psi_0, \quad (2.27)$$

where

$$\phi_-(k, 1/2) = \int_{-\infty}^0 \phi(x, 1/2) e^{ikx} dx \quad \text{and} \quad \psi_-(k, 1/2) = \int_{-\infty}^0 \psi(x, 1/2) e^{ikx} dx, \quad (2.28)$$

and ψ_0 denotes the finite value of $\psi(x, y)$ at the position $(0, 1/2)$. Substituting (2.19) and (2.22) into (2.27), we obtain

$$D(k, 1/2) = -i\omega\sigma\phi^*(k) e^{-\gamma_1(k)/2} - (-i\omega - ik)\psi_s^*(k) \sinh \gamma_2(k)/2. \quad (2.29)$$

Combining (2.23), (2.25), (2.27), and (2.29) yields

$$\phi'_+(k, 1/2) + \frac{iG}{k - i\epsilon} = K(k) F_-(k), \quad (2.30)$$

where

$$K(k) = \frac{1}{\frac{\sigma}{\gamma_1(k)} + \frac{(1 + k/\omega)^2 \tanh \gamma_2(k)/2}{\gamma_2(k)}}, \quad (2.31)$$

$$F_-(k) = (1 + k/\omega)\psi_-(k, 1/2) - \sigma\phi_-(k, 1/2) - i\psi_0/\omega. \quad (2.32)$$

Equation (2.30) represents the Wiener-Hopf equation we aim to solve, with the kernel given by $K(k)$. $1/K(k) = 0$ represents the dispersion relation of the antisymmetric mode of the jet instability wave. It can be seen that as $|k| \rightarrow \infty$, $|K(k)| \rightarrow |k|^{-1}$. Now, following the procedures of the Wiener-Hopf method, we assume that the kernel can be decomposed into

$$K(k) = K_+(k)K_-(k), \quad (2.33)$$

where $K_+(k)$ and $K_-(k)$ are analytic and non-zero in the upper and lower half-planes of k , respectively. Meanwhile, both $K_+(k)$ and $K_-(k)$ behave as $O(k^{-1/2})$ as k approaches infinity. The actual decomposition will be shown in section 2.2. Routine use of Wiener-Hopf decomposition leads to

$$\frac{\phi'_+(k, 1/2)}{K_+(k)} + \left(\frac{1}{K_+(k)} - \frac{1}{K_+(i\epsilon)} \right) \frac{iG}{k - i\epsilon} = E(k), \quad (2.34)$$

$$K_-(k)F_-(k) - \frac{1}{K_+(i\epsilon)} \frac{iG}{k - i\epsilon} = E(k). \quad (2.35)$$

Here $E(k)$ is an entire function of k . Due to the Kutta condition (Crighton 1985), $\phi(x, 1/2)$ behaves like $x^{3/2}$ near the nozzle lip. The corresponding value of $\phi'(x, 1/2)$ is therefore $O(x^{1/2})$. It follows that $\phi'_+(k, 1/2) \rightarrow k^{-3/2}$ as $k \rightarrow \infty$ (Erfelyi 1958). Thus, from Liouville's theorem,

$$E(k) \equiv 0. \quad (2.36)$$

From (2.23) and (2.34), $\phi'(k, 1/2)$ can be readily solved, i.e.

$$\phi'(k, 1/2) = \frac{iG}{k - i\epsilon} \frac{K_+(k)}{K_+(i\epsilon)}. \quad (2.37)$$

It can be seen that $\phi'(k, 1/2)$ is $O(k^{-3/2})$ as $|k|$ approaches infinity in the upper half plane. The corresponding velocity component $\phi'(x, y)$ behaves as $x^{1/2}$ when $x \rightarrow 0$, which leads to singularity in $\psi'(x, y)$ due to (2.15). Therefore, (2.37) leads to singular behaviour when $|k| \rightarrow \infty$, where (2.37) can be approximated by (Crighton 1992)

$$\frac{iG}{K_+(i\epsilon)} \frac{K_+(k)}{k}. \quad (2.38)$$

This part will be further discussed in section 2.3, where the unsteady Kutta condition is used to determine the new instability wave by removing the emerging singularity.

2.2. The kernel decomposition

In this section, we factor the kernel $K(k)$ into $K_+(k)$ and $K_-(k)$, which is the essential step of the Wiener-Hopf technique. Before proceeding with the decomposition of the kernel, it is necessary to properly define the branch cuts of $K(k)$. In order to ensure that the real part of γ_1 is positive as $|k| \rightarrow \infty$ along the integration path (which becomes relevant when conducting the inverse Fourier transform if we are interested in calculating

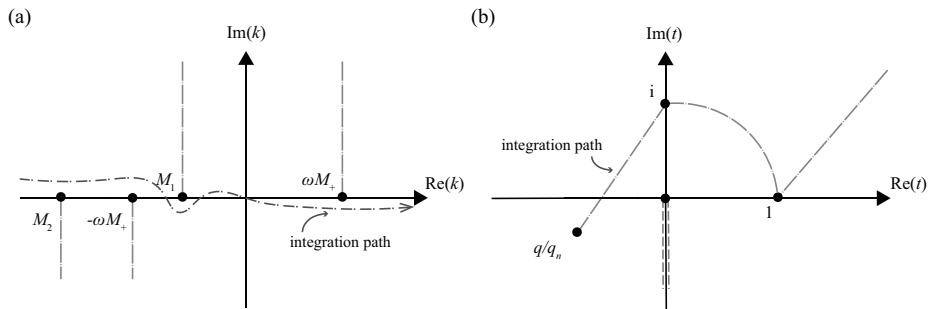


FIGURE 2. (a) Schematic of the branch points, branch cuts, and the integration path in the complex k plane. (b) Schematic of the deformed integration path in the complex t plane.

the scattered sound field), the branch cuts of γ_1 passing the branch points $k = \pm\omega M_o$ are chosen to extend to the upper and lower half-plane, respectively, as shown in figure 2(a). The branch is selected in such a way that $\arg(\gamma_1) = -\pi/2$ at $k = i$. On the other hand, the branch points of γ_2 are determined as $M_1 = -\omega M_i/(M_i + 1)$ and $M_2 = -\omega M_i/(M_i - 1)$. The branch cuts passing M_1 and M_2 are chosen to extend to the lower and upper half-plane, respectively, for the convenience of the kernel decomposition. The branch of γ_2 is selected to ensure that $\arg(\gamma_2) = -\pi/2$ at $k = i$. Due to the choice of the branch cuts, we can find that $\gamma_2(k)/\gamma_1(k) \rightarrow \sqrt{1 - M_i^2}$, as $\omega \rightarrow 0$ and $k \rightarrow O(1)$.

The kernel can be rewritten as

$$K(k) = \frac{\gamma_2(k)}{\sigma\gamma_2(k)/\gamma_1(k) + (1 + k/\omega)^2 \tanh \gamma_2(k)/2}. \quad (2.39)$$

A proper decomposition of $\gamma_2(k)$ is evident, i.e. $\gamma_2(k) = \sqrt{k - M_1}\sqrt{k - M_2}$. Thus, in what follows we only focus on the denominator, which we refer to as $Q(k)$. It can be seen that $Q(k)$ depends on the dispersion relation of the antisymmetric mode of the jet instability wave. This dispersion relation describes several types of waves present in the jet, determined by its structural characteristics such as branches, zeros, and poles. These information can be maintained if the kernel is decomposed by means of matched asymptotic expansions (Crighton 1992, 2001). To use this strategy, a small parameter should be specified as the basis for the expansion. This parameter should not only be small but can also be contained by the kernel. We introduce $S = \omega(M_i - 1)^2$ as this parameter. In what follows, the complicated kernel is replaced by a simpler one by asymptotic expansions based on S . Overlapping approximations are subsequently applied to guarantee the validity of the decomposition over the whole range of the wavenumber k . The final result is obtained by a multiplicative composite approximation.

We first assume $k = O(1)$ and let $\omega \rightarrow 0$. The first term of $Q(k)$, i.e. $\sigma\gamma_2(k)/\gamma_1(k)$ reduces to $\sigma\sqrt{1 - M_i^2}$ and $Q(k)$ can be approximated as

$$Q(k) \approx \left(\frac{k}{\omega}\right)^2 \tanh \sqrt{(1 - M_i^2)k^2}/2. \quad (2.40)$$

The term $\sqrt{(1 - M_i^2)k^2}$ is supposed to maintain the branch cut chosen for $\gamma_2(k)$. For

brevity, we rewrite $\sqrt{(1 - M_i^2)k^2}$ as $\sqrt{1 - M_i^2}k^*$, where the script $*$ represents that this parameter retains the specified branch cuts.

Now, we introduce the small parameter $S = \omega(M_i - 1)^2$ and a new scaled wavenumber according to

$$q = k/S^{\frac{3}{4}}. \quad (2.41)$$

By assuming $S \rightarrow 0$ and $q \rightarrow O(1)$, we can expand $Q(k)$ in (2.39) based on the small parameter S (using methods of Taylor expansion), i.e.

$$Q(k) \approx \sqrt{1 - M_i^2} \left(\sigma - \frac{\sigma M_i^2 S^{1/4}}{(M_i - 1)^2 (1 - M_i^2) q^*} + \frac{1}{2} (M_i - 1)^4 S^{1/4} q^2 q^* \right), \quad (2.42)$$

where $q^* = k^*/S^{\frac{3}{4}}$. Note that despite the small parameter $S \sim o(1)$, the quantities $S^{1/4} \sim O(1)$. To put this into perspective, let us consider an example with $M_i = 1.1$. At the screech frequency, employing Powell's original model yields $S = 0.028$. However, $S^{1/4} = 0.41$, which is of the order of unity. The scale separation can be shown more clearly as M_i increases. This demonstrates that although S itself may be small, its corresponding fractional power can still have magnitudes of the order of unity in our interested application.

We can show that (2.40) and (2.42) do overlap, as $k \rightarrow 0$ and $q \rightarrow \infty$, respectively, with common value $\frac{1}{2} \sqrt{1 - M_i^2} (M_i - 1)^4 S^{1/4} q^2 q^*$. A multiplicative composite approximation then reads

$$Q(k) \approx \sqrt{1 - M_i^2} \frac{\tanh \frac{1}{2} \sqrt{1 - M_i^2} k}{\frac{1}{2} \sqrt{1 - M_i^2} k} \frac{1}{q^*} R(q), \quad (2.43)$$

where

$$R(q) = \sigma q^* - \frac{\sigma M_i^2 S^{1/4}}{(M_i - 1)^2 (1 - M_i^2)} + \frac{1}{2} (M_i - 1)^4 S^{1/4} q^4. \quad (2.44)$$

To validate the decomposition, the wavenumber obtained by letting $Q(k)$ in (2.43) equal to 0, which corresponds to the wavenumber of the sinuous mode of the jet instability wave, is compared to that numerically solved by the dispersion relation $1/K(k) = 0$. As shown in figure 3, the agreement between the two wavenumbers is good when $M_i > 1.2$. Therefore, in the subsequent analysis, our focus will be in the range of $M_i > 1.2$.

We are now in a position to factor the function $Q(k)$. From Noble (1956), $\frac{\tanh \sqrt{1 - M_i^2} k/2}{\sqrt{1 - M_i^2} k/2}$ can be decomposed to

$$\frac{\tanh \frac{1}{2} \sqrt{1 - M_i^2} k}{\frac{1}{2} \sqrt{1 - M_i^2} k} = T_+(k) T_-(k), \quad (2.45)$$

where

$$T_+(k) = \frac{\Gamma(1/2 + \sqrt{M_i^2 - 1} k/2\pi)}{\pi^{1/2} \Gamma(1 + \sqrt{M_i^2 - 1} k/2\pi)}, \quad T_-(k) = \frac{\Gamma(1/2 - \sqrt{M_i^2 - 1} k/2\pi)}{\pi^{1/2} \Gamma(1 - \sqrt{M_i^2 - 1} k/2\pi)}. \quad (2.46)$$

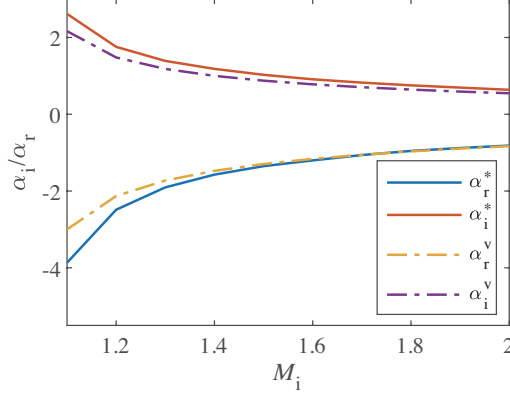


FIGURE 3. Comparison between the wavenumbers of the sinuous mode of the jet instability wave obtained by the decomposed kernel (2.43) and the dispersion relation. α^* and α^v denote the wavenumber calculated from the decomposed kernel and $M(k)$, respectively, while the subscript r and i represent the real and imaginary part of the parameter, respectively. σ is assumed to be 1.

Here Γ represents the Gamma function. The decomposition of $1/q^*$ reads

$$\frac{1}{q^*} = \mathcal{Q}_+(q)\mathcal{Q}_-(q), \quad (2.47)$$

where

$$\mathcal{Q}_+(q) = \frac{1}{\sqrt{q+0}}, \quad \mathcal{Q}_-(q) = \frac{1}{\sqrt{q-0}}. \quad (2.48)$$

Naturally, the branch cut of \mathcal{Q}_+ and \mathcal{Q}_- is from -0 to $-\infty$ and from $+0$ to $+\infty$, respectively.

The decomposition of $R(q)$, on the other hand, is very difficult due to the presence of q^* in (2.44). To decompose $R(q)$, we let q be real first (Crighton 1992), so that $q^* = |q|$. This is reasonable considering that the overlap of the two half-planes will converge to the real axis in the complex k plane. Assuming that $R(q)$ can be decomposed to $R(q) = R_+(q)R_-(q)$, and taking the first derivative of $\ln R(q)$, we obtain

$$\frac{d}{dq} \ln R_+(q) + \frac{d}{dq} \ln R_-(q) = \frac{4q^3 + a_1|q|/q}{q^4 + a_1|q| + a_0}, \quad (2.49)$$

where

$$a_0 = 2\sigma M_i^2 (M_i - 1)^{-6} (M_i^2 - 1)^{-1},$$

$$a_1 = 2\sigma (M_i - 1)^{-4} S^{-1/4}.$$

Multiplying the numerator and the denominator of the right-hand side term in (2.49) by $q^4 - a_1|q| + a_0$, equation (2.49) can be written as

$$\frac{d}{dq} \ln R_+(q) + \frac{d}{dq} \ln R_-(q) = \frac{(4q^3 + a_1|q|/q)(q^4 - a_1|q| + a_0)}{(q^4 + a_0)^2 - a_1^2 q^2}. \quad (2.50)$$

The zeros of the denominator $(q^4 + a_0)^2 - a_1^2 q^2$ are defined as $q_n, n = 1, \dots, 8$, which

can be obtained by Ferrari's formula. The details are provided in Appendix A. With the knowledge of these zeros, we can now reorganize (2.50) as

$$\begin{aligned} \frac{d}{dq} \ln \left(\frac{R_+(q)}{\prod_{n=5}^8 (q - q_n)^{1/2}} \right) + \frac{d}{dq} \ln \left(\frac{R_-(q)}{\prod_{n=1}^4 (q - q_n)^{1/2}} \right) \\ = \sum_{n=1}^4 \xi_n \frac{|q|}{(q - q_n)} + \sum_{n=5}^8 \xi_n \frac{|q|}{(q - q_n)} + \frac{a_1}{a_0} \frac{|q|}{q}, \end{aligned} \quad (2.51)$$

where

$$\xi_n = \frac{-3a_1 q_n^4 + a_0 a_1}{2q_n^2 (4q_n^6 + 4a_0 q_n^2 - a_1^2)}. \quad (2.52)$$

The detailed derivation from (2.50) to (2.51) can be found in Appendix B. For brevity, we can define $\xi_9 = a_1/a_0$ and $q_9 = 0$. With these definitions, it is straightforward to find

$$\sum_{n=1}^9 \xi_n q_n = \sum_{n=1}^9 \xi_n = 0. \quad (2.53)$$

An additive decomposition of $|q|$ is now introduced, i.e.

$$|q| = Q_+(q) + Q_-(q), \quad (2.54)$$

where

$$Q_+(q) = q/2 + \frac{iq}{\pi} \ln_+ q, \quad Q_-(q) = q/2 - \frac{iq}{\pi} \ln_- q. \quad (2.55)$$

The branch cuts of \ln_+ and \ln_- extend from 0 to $-\infty$ and from 0 to $+\infty$, respectively. The choice of the branch cut leads to

$$Q_+(q) = Q_-(-q). \quad (2.56)$$

Using the additive decomposition (2.54) and the two identities (2.53) and (2.56), the right-hand side of (2.51) can obtain a similar additive factorization, and $R_+(q)$ can be finally found as

$$R_+(q) = \prod_{n=5}^8 (q - q_n)^{1/2} \exp \left(-\frac{i}{\pi} \sum_{n=1}^8 \xi_n q_n \int_{q/q_n}^{\infty} \frac{\ln_+ t}{t-1} dt + \sum_{n=5}^8 \xi_n q_n \int_{q/q_n}^{\infty} \frac{1}{t-1} dt \right). \quad (2.57)$$

The detailed derivation from (2.51) to (2.57) can be found in Appendix B.

To evaluate the integral in (2.57), as shown in figure 2(b), we deform the integration path in (2.57) from q/q_n to the point $e^{\pi i/2}$, then along a unit circle to reach $q/q_n = 1$ situated on the real axis, and finally along a ray from $q/q_n = 1$ to ∞ . Using the identity (2.53), we can evaluate (2.57) to obtain

$$R_+(q) = \prod_{n=5}^8 (q - q_n)^{1/2} \exp \left(-\frac{i}{\pi} \sum_{n=1}^8 \xi_n q_n \text{Li}_2(1 - q/q_n) - \sum_{n=5}^8 \xi_n q_n \ln_+ \frac{q}{q_n} \right). \quad (2.58)$$

Here Li_2 represents the polylogarithm function of the second order (Gradshteyn & Ryzhik 1980).

Using (2.46), (2.48), and (2.58) we obtain the final form of K_+ , i.e.

$$K_+(k) = \frac{\sqrt{k - M_2}}{T_+(k)R_+(k/S^{3/4})Q_+(k/S^{3/4})}. \quad (2.59)$$

A complete expression of K_+ is ,

$$K_+(k) = \sqrt{\pi} \frac{\Gamma(1 + \sqrt{M_1^2 - 1}k/2\pi)}{\Gamma(1/2 + \sqrt{M_1^2 - 1}k/2\pi)} \frac{\sqrt{k - M_2} \sqrt{k/S^{3/4} + 0}}{\prod_{n=5}^8 (q - q_n)^{1/2}} \exp\left(\frac{i}{\pi} \sum_{n=1}^8 \xi_n q_n \text{Li}_2(1 - q/q_n) + \sum_{n=5}^8 \xi_n q_n \ln_+ \frac{q}{q_n}\right). \quad (2.60)$$

As $k \rightarrow 0$, the Taylor expansion of $K_+(k)$ reduces to

$$K_+(k) \approx \frac{i\pi\sqrt{M_2}}{\mathcal{C}S^{3/8}} \sqrt{k} + O(k^{3/2}). \quad (2.61)$$

Here, the constant \mathcal{C} is defined as $\mathcal{C} = \prod_{n=5}^8 q_n^{1/2}$. Equation (2.61) will be used to determine ϵ in section 2.3.

2.3. Instability waves excited by the acoustic waves at the nozzle lip

Under the excitation of the acoustic wave, new instability waves would emerge near the nozzle lip (Crighton 1985). We can determine this instability wave by imposing the unsteady Kutta condition at the nozzle lip (Crighton 1981). Following Crighton (1972) and considering that we focus on the upper half-plane ($y > 1/2$), we assume that the excited instability wave can be represented by

$$\phi^* = \mathcal{A}e^{-i\mathcal{K}x - \gamma(\mathcal{K})y}, \quad (2.62)$$

where \mathcal{A} represents the amplitude of the instability wave and $\gamma(\mathcal{K})$ is defined by $\gamma(\mathcal{K}) = \sqrt{\mathcal{K}^2 - \omega^2 M_0^2}$. The parameter \mathcal{K} denotes the wavenumber of the instability waves of the antisymmetric mode, and its determination is outlined in Appendix A. The choice of the form in (2.62) is believed to be reasonable, particularly considering the sinuous nature exhibited by both the upstream forcing and the scattered acoustic field.

The instability wave then propagates downstream and subsequently interacts with the shock structures (Powell 1953*b*; Suda *et al.* 1993; Edgington-Mitchell *et al.* 2021). This interaction leads to the emission of sound, which serves as the upstream forcing and completes the screech feedback loop. To determine the instability amplitude \mathcal{A} in (2.62), we first calculate the scattered field resulting from the newly-excited instability wave at the nozzle lip. The singular component within the resulting scattered field needs to be eliminated using the singularity in (2.38). This process fixes the value of \mathcal{A} in order to satisfy the unsteady Kutta condition.

Replacing the forcing term GY in (2.9) and (2.10) with ϕ^* while following the same procedures outlined in section 2.1, we obtain the scattered field due to the presence of

the instability wave, i.e.

$$\phi_+^{*'}(k, 1/2) = \frac{i\mathcal{A}\gamma(\mathcal{K})e^{-\gamma(\mathcal{K})/2}}{k - \mathcal{K}} \left(1 - \frac{K_+(k)}{K_+(\mathcal{K})}\right), \quad (2.63)$$

The component of $\phi_+^{*'}(k)$ similar to (2.38) that leads to singularity is

$$-\frac{i\mathcal{A}\gamma(\mathcal{K})e^{-\gamma(\mathcal{K})/2}}{K_+(\mathcal{K})} \left(\frac{K_+(k)}{k}\right). \quad (2.64)$$

The unsteady Kutta condition demands no singularity in the vicinity of $r \rightarrow 0$, therefore from (2.38) and (2.64) we must have

$$\frac{iG}{K_+(i\epsilon)} - \frac{i\mathcal{A}\gamma(\mathcal{K})e^{-\gamma(\mathcal{K})/2}}{K_+(\mathcal{K})} = 0. \quad (2.65)$$

The parameter G and the kernel function K_+ are defined by (2.7) and (2.59), respectively. To evaluate \mathcal{A} , we need to determine the small parameter ϵ , which seems to be an arbitrary value introduced to address the issue of non-convergence. However, ϵ in fact has a physic-imposed value and we may uniquely determine it by re-evaluating the problem without approximations.

First, replace the forcing term GY in (2.9) and (2.10) by

$$F(h) = \frac{1}{2\pi} \int_{-\infty}^{\infty} D_o(\lambda) \exp(-i\lambda h) d\lambda. \quad (2.66)$$

Then the Wiener-Hopf equation (2.30) takes a new form, i.e.

$$\phi_+^{*'}(k, 1/2) + \mathcal{F}(k) = K(k)F_-(k). \quad (2.67)$$

Here

$$\mathcal{F}(k) = \int_{-\infty}^0 \int_0^{\infty} \mathcal{G}(\zeta^*) \exp(\zeta^* x) e^{ikx} d\zeta^* dx, \quad (2.68)$$

where $\zeta^* = -i\lambda$, and the form of $\mathcal{G}(\zeta^*)$ is shown in Appendix B. If we intend to completely account for the effect of the upstream forcing, we can replace G by $\mathcal{G}(\zeta^*)$ and ϵ by ζ^* , and then carry out the integration from 0 to ∞ . The mathematical proof of this procedure can be found in Appendix C. Thus, it follows that

$$\frac{G}{K_+(i\epsilon)} = \int_0^{\infty} \frac{\mathcal{G}(\zeta^*)}{K_+(i\zeta^*)} d\zeta^*. \quad (2.69)$$

The integration on the right-hand side of (2.69) can be evaluated using Watson's Lemma. On the left-hand side of (2.69), given that ϵ is a small term, $K_+(i\epsilon)$ can be evaluated employing its Taylor expansion. By combining (2.61) and (C6), we have

$$\epsilon = -\frac{iG^2 h^3}{\pi \mathcal{G}^2(0)}. \quad (2.70)$$

To verify that ϵ is a small term, we calculate it using (2.70) and plot it in figure 4. The angular frequency of the instability wave is calculated using the original formula (1.1) proposed by Powell (1953a). Figure 4 shows that within the range of $1.2 < M_i < 2$,

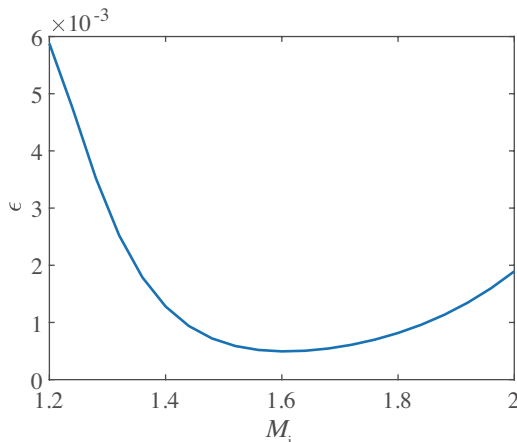


FIGURE 4. The value of the parameter ϵ in the range of $1.2 < M_i < 2$ at the screeching frequency. The frequency is obtained by the original formula (1.1) proposed by Powell (1953a).

the value of ϵ initially decreases from its maximal value of 5.9×10^{-3} at $M_i = 1.2$ to 4.9×10^{-4} at $M_i = 1.6$, and then gradually increases to around 1.9×10^{-3} at $M_i = 2$. In the entire Mach number region, ϵ is small, ensuring the validity of using Taylor expansion in (2.61) and the omission of $G\epsilon/\omega$ in (2.25).

Having obtained all the parameters, the instability wave is found to be

$$\phi^*(0, 1/2) = \frac{GK_+(\mathcal{K})}{\gamma(\mathcal{K})K_+(i\epsilon)}. \quad (2.71)$$

This equation enables us to define the important transfer function, i.e.

$$H(\omega, M_i, \nu) = \frac{K_+(\mathcal{K})}{\gamma(\mathcal{K})K_+(i\epsilon)}, \quad (2.72)$$

where K_+ is given by (2.59), \mathcal{K} by (A 7), $\gamma(\mathcal{K}) = \sqrt{\mathcal{K}^2 - \omega^2 M_0^2}$, and ϵ by (2.70). This transfer function describes the linear mapping between the newly-excited instability waves and the upstream propagating acoustic waves. Using this function, both the scattering efficiency and the phase delay between these two waves can be readily examined.

3. Results

We first investigate the behaviour of the transfer function H under two typical screech conditions, i.e. $M_i = 1.3$ and $M_i = 1.5$. We also consider the effects of the temperature by showing results at three temperature ratios, i.e. $\nu = 1, 2$, and 3 . The amplitude, i.e. the scattering efficiency, and the phase of H are shown in figure 5. Note that the phase is defined in the range $0 \leq \arg(H) < 2\pi$. Considering that the asymptotic expansion yields favourable approximation when $M_i > 1.2$, which corresponds to screech frequency within the range of $1 < \omega < 3$, only the frequency range from 1 to 3 is examined. Figures 5(a) and 5(c) show that the scattering efficiency $|H|$ displays multiple peaks and valleys as

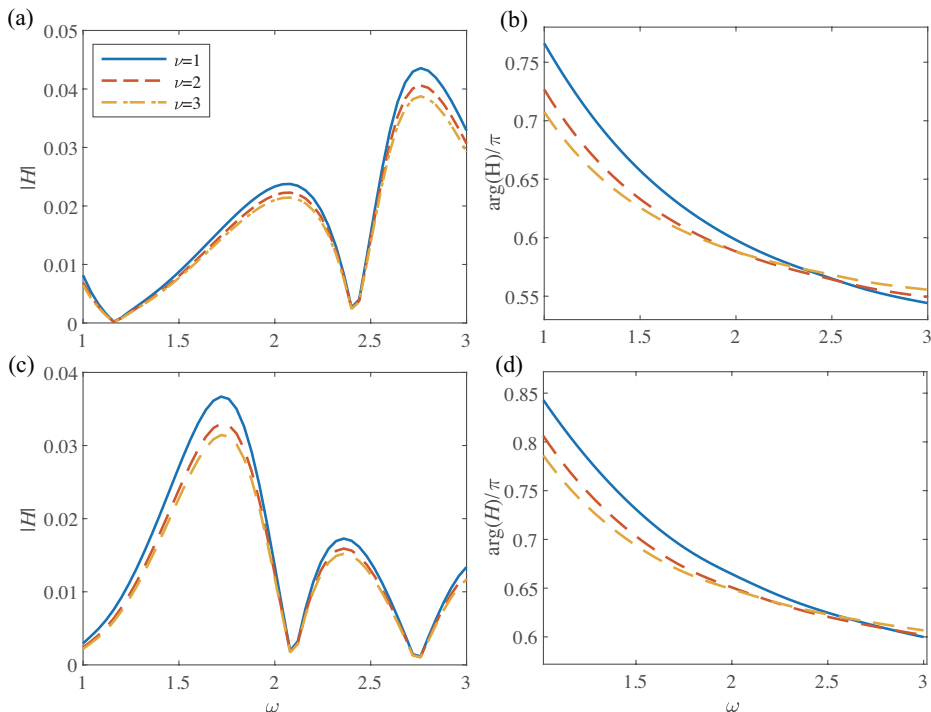


FIGURE 5. The amplitude and phase of the transfer function $H(\omega, M_1, \nu)$. The jet Mach number M_1 is 1.3 and 1.5 in (a)-(b) and (c)-(d) respectively. The transfer function is examined under three temperature conditions, i.e. $\nu = 1, 2$, and 3.

the frequency varies. In both cases, $|H|$ is less than 5% and decreases to 2‰ at certain frequencies. Note that the temperature has a mild impact on the scattering efficiency. Specifically, as the temperature ratio increases, the scattering efficiency decreases slightly. Regarding the phase delay, figures 5(b) and 5(d) show a phase delay between around $\pi/2$ to $4\pi/5$, which demonstrates a decreasing trend as the frequency increases. In addition, higher jet temperatures lead to lower phase delays at low frequencies while resulting in slightly higher phase delays at high frequencies.

3.1. Phase condition for jet screech

Using the transfer function, we can examine the phase condition for the screech feedback loop in this section. In the subsequent analysis, we first focus on the cold jet, which corresponds to the operation conditions commonly employed in experiments and numerical simulations. We then incorporate the thermal influence to account for temperature effects on the screech frequency.

The original phase condition proposed by Powell (1953a) can be written as

$$\frac{N - \Delta}{f} = \frac{h}{|U^+|} + \frac{h}{|U^-|}, \quad (3.1)$$

where U^+ and U^- represent the nondimensional phase velocity of the downstream-

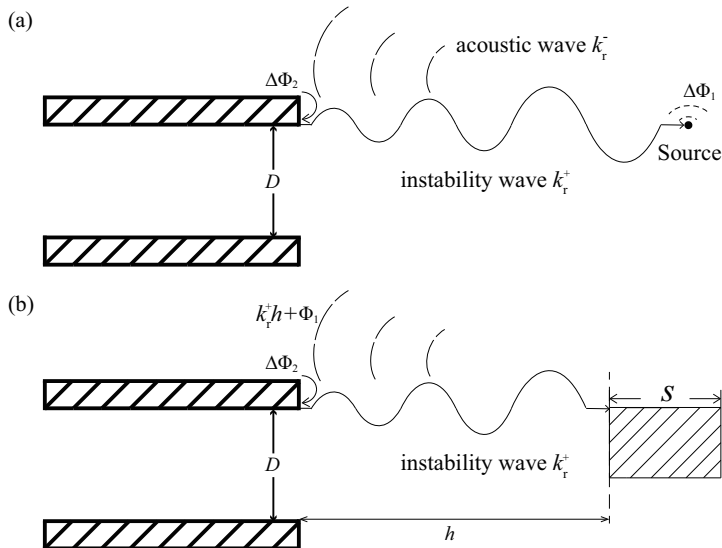


FIGURE 6. Schematics of the phase condition for the feedback loop of jet screech. (a) Powell's model; (b) this model.

propagating instability waves and the upstream-propagating acoustic waves, respectively. Note that $U^- = 1/M_0$ in this study. The integer N denotes the total number of phase cycles contained in the feedback loop, and Δ represents a number between 0 and 1 due to the additional phase delay. Note that this phase criterion can be reformulated, as demonstrated by Jordan *et al.* (2018) and Mancinelli *et al.* (2021), in the following manner, i.e.

$$(|k_r^+| + |k_r^-|)h + \Delta\phi = 2\pi N, \quad (3.2)$$

where k_r^+ and k_r^- are, respectively, the real part of the wavenumber of the downstream-propagating instability waves and the upstream-propagating acoustic waves. The term $\Delta\phi$ is defined as $2\pi\Delta$ and represents the additional phase delay. As illustrated in figure 6(a), the instability wave with the wavenumber k_r^+ grows spatially from the nozzle lip to the effective source location and interacts with the shock structure. This interaction produces acoustic waves, which propagate to the upstream direction with the wavenumber k_r^- and trigger new instability waves at the nozzle lip. The total phase variations during this feedback loop must be equal to an integer multiplied by 2π . Therefore, the phase condition can be written as (3.2). As illustrated in figure 6(a), the total phase delay $\Delta\phi$ consists of two components: the phase change occurring during the sound emission ($\Delta\phi_1$) and that during the jet receptivity ($\Delta\phi_2$).

To predict the screech frequency, the parameters contained in (3.2), such as k_r^+ , k_r^- , and $\Delta\phi$ should be specified, respectively. Regarding k_r^+ , it is commonly assumed that the phase velocity of the jet instability waves U_c is proportional to the velocity of the

fully expanded jet flow. Therefore, we can write k_r^+ as

$$k_r^+ = \frac{\omega}{\kappa}, \quad (3.3)$$

where κ typically falls within the range of 0.5 to 0.8, and its value depends on factors such as the nozzle shape and the jet Mach number. In circular nozzles, a value of $\kappa = 0.7$ may be used (Harper-Bourne & Fisher 1973). However, studies by Li & Gao (2010) have indicated that κ may vary with the jet Mach number. In the case of a rectangular jet, experiments suggested that values between 0.5 and 0.65 may be more appropriate compared to 0.7 (Powell 1953*a*; Krothapalli *et al.* 1986; Raman & Rice 1994; Panda *et al.* 1997). Similarly, variations in κ due to changes in jet Mach numbers have also been reported (Powell 1953*a*; Panda *et al.* 1997).

Based on experimental measurements and data analysis, Tam & Reddy (1996) proposed an empirical formula to estimate κ for rectangular nozzles, i.e.

$$\kappa = 0.5 + 0.2e^{-0.5(\Lambda-1)}, \quad (3.4)$$

where Λ is the aspect ratio of the rectangular nozzle. For a high-aspect-ratio rectangular jet, Tam & Reddy (1996) and Berland *et al.* (2007) applied the value of $\kappa = 0.55$. In the rest of this paper, if no specific data is available, we use this empirical formula to determine κ .

For k_r^- , it is straightforward to find that

$$|k_r^-| = \omega M_o = \omega M_c / \kappa. \quad (3.5)$$

Combining (2.5), (3.2), (3.3), and (3.5) yields

$$f = \frac{2\pi N - \Delta\phi}{2\pi n} \frac{\kappa}{s(1 + M_c)}. \quad (3.6)$$

Note that, the additional phase delay $\Delta\phi$ is typically assumed to be 0 in previous studies (Jordan *et al.* 2018; Li *et al.* 2023). The integer N , according to the findings of Mercier *et al.* (2017), is often equal to the shock cell number n for circular nozzles. We assume that this relation holds for the two-dimensional jet under consideration. By setting $\Delta\phi = 0$ and $N = n$, equation (3.6) can be simplified to (1.1), which represents the original frequency prediction model proposed by Powell (1953*a*). Note that (1.1) is derived under the assumption that the sound intensity in the upstream direction reaches its maximum, thus corresponding to the constructive interference condition. We can see that the frequency prediction formula obtained from the phase condition coincides with (1.1) when $\Delta\phi = 0$ and $N = n$.

As we can see from figure 6(a), an effective screech source is assumed in early research on the phase condition. However, whether the screech source is distributed or localized is still open to debate. As illustrated in figure 6(b), in our previous study (Li & Lyu 2023), the acoustic wave is generated by the interaction between the instability wave and the distributed shock cells. Consequently, the sound source is distributed across

Cases	κ	A	M_d	ν	N	N^*
Powell (1953a)	0.6	5.83	1	1	4	3
Raman & Rice (1994)	0.54	9.63	1	1.42	4	3
Panda <i>et al.</i> (1997)	0.65	5	1	1	4	3
Alkislar <i>et al.</i> (2003)	0.63	4	1.44	1	4	3

TABLE 1. The operation conditions used in several experiments.

various shock structures, e.g. the fourth and fifth shock structures. Therefore, we cannot pinpoint a specific point source. Nevertheless, without an effective source location, we can still establish a phase condition in this model, i.e.

$$k_r^+ h + \Phi_1 + \Delta\Phi_2 = 2\pi N^*. \quad (3.7)$$

Here, h denotes the distance between the nozzle lip and the left boundary of the source region as shown in figure 6(b). Φ_1 represents the phase of the resulting acoustic wave at the nozzle lip, which is generated from the interaction between the shock structures and an instability wave whose phase is set to be 0 at the left boundary of the source region. The actual phase of the acoustic wave at the nozzle lip, after taking account of the phase variation due to instability propagation, would be $k_r^+ h + \Phi_1$, as shown in figure 6(b). $\Delta\Phi_2$ denotes the phase change during the jet receptivity, which is the same as that defined in figure 6(a). Similar to (3.2), the total phase variations during the feedback loop should be equal to an integer multiplied by 2π . Therefore, we can write the phase condition as (3.7), where a new integer N^* is introduced. We expect $N^* < N$ because the actual phase variation between the left boundary of the source region and the nozzle lip is probably more than 2π . However, only Φ_1 is included, which is less than 2π under several operation conditions. We find that $N^* = N - 1$ is often appropriate. From (3.3) and (3.7), we can obtain

$$f = \frac{2\pi N^* - \Phi_1 - \Delta\Phi_2}{2\pi ns} \kappa. \quad (3.8)$$

Equipped with $\Delta\Phi_2$ obtained from the transfer function and Φ_1 obtained from Li & Lyu (2023), we can compare this model prediction with Powell's model prediction and the experimental measurements.

The operation conditions used in four experiments in the open literature, including the aspect ratio of the rectangular nozzle (A), the designed Mach number of the nozzle (M_d), and the temperature ratio (ν) are listed in table 1. In these experiments, the convection velocities of the instability wave were all measured. The constants κ obtained from these experiments are listed in table 1. Note that in Panda *et al.* (1997), the constant κ was found to increase as M_i increased, from 0.6 at low M_i to 0.7 at high M_i . We use an average value of 0.65 to initiate the computation. In addition, the screech source region was reported to be around the fourth shock structure from experimental observations,

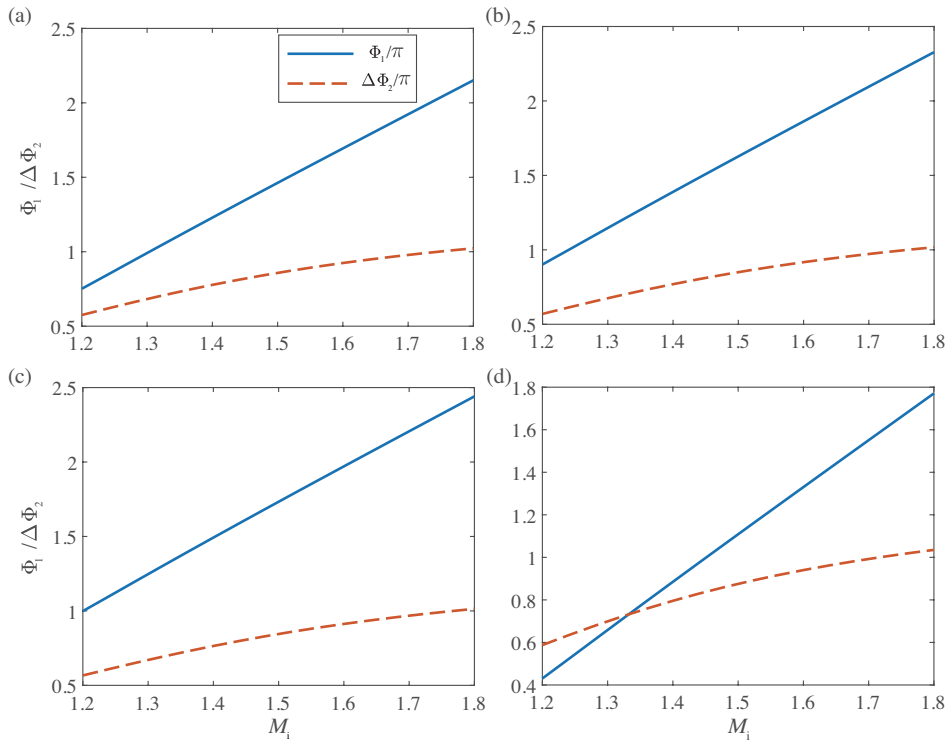


FIGURE 7. The phase changes Φ_1 and $\Delta\Phi_2$ at the screeching frequency. The operation conditions used in figures with labels (a)-(d) are the same as those used in Powell (1953*b*), Raman & Rice (1994), Panda *et al.* (1997), and Alkislar *et al.* (2003), respectively.

thus we set $N = 4$ and $N^* = 3$ in the four cases. To calculate the shock spacing s in (3.6) and (3.8), we use the model proposed by Tam (1988), where s can be expressed by

$$s = 2\sqrt{M_1^2 - 1} \left[\left(\frac{1}{W} \right)^2 + 1 \right]^{-\frac{1}{2}}. \quad (3.9)$$

Here W represent the nondimensional height and width of the fully expanded jet flow. $1/W$ is related to the jet aspect ratio (Λ), the Mach number of the fully expanded jet flow (M_1), and the designed Mach number (M_d). The method to calculate $1/W$ can be found in Tam (1986).

The phase Φ_1 and the phase delay $\Delta\Phi_2$ can be readily calculated if f is provided. However, f depends on Φ_1 and $\Delta\Phi_2$ via (3.8). So to determine Φ_1 and $\Delta\Phi_2$ in (3.8), we use an iterative scheme as follows. We first employ the operation conditions presented in table 1 and calculate the screech frequency using Powell's original formula (1.1). Subsequently, the obtained frequency is substituted into this model to determine Φ_1 and $\Delta\Phi_2$. A new screech frequency can then be predicted using (3.8). This new frequency can be used to obtain an updated Φ_1 and $\Delta\Phi_2$. The procedures are repeated until a converged frequency is obtained. We first show the phase changes in figure 7. As can be seen, both Φ_1 and $\Delta\Phi_2$ increase as the jet Mach number increases. Φ_1 increases in a nearly linear

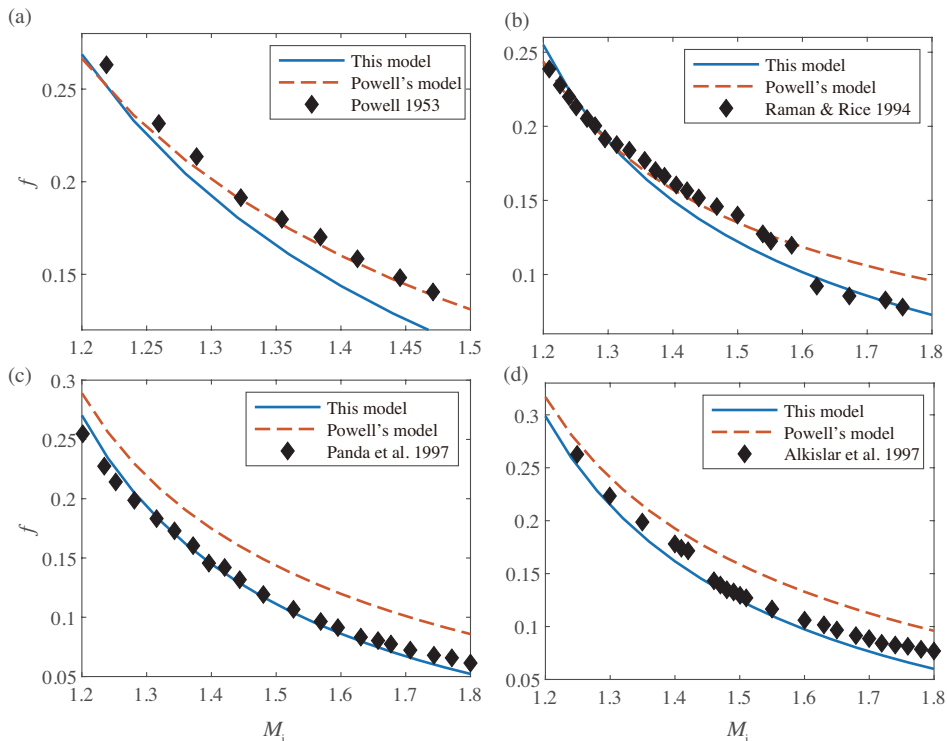


FIGURE 8. Comparison between Tam’s model prediction, this model prediction, and the experimental data. The solid blue curve is calculated by Powell’s model. The dashed red line is obtained using this model. Experimental data in figures with label (a)-(d) are measured by Powell (1953*b*), Raman & Rice (1994), Panda *et al.* (1997), and Alkislar *et al.* (2003), respectively.

manner with respect to M_i , while $\Delta\Phi_2$ varies slowly as M_i changes, increasing from nearly $\pi/2$ at low Mach numbers to π as M_i increases to 1.8.

Equipped with the Φ_1 and $\Delta\Phi_2$, we can calculate f from (3.8). Comparison between this model prediction, Powell’s model prediction, and the experimental data are shown in figure 8. It can be seen that this model predictions agree well with the experimental data in figures 8(c)-(d), while Powell’s model predictions seem to show an overprediction compared to the experiments. Note that in figure 8(c), setting $\kappa = 0.5$ can lead to favourable agreement between Powell’s model prediction and the experimental data, as shown by Berland *et al.* (2007), whereas using the convection velocity directly obtained from the experimental data leads to an overprediction. In figure 8(a), on the other hand, this model underpredicts the screech frequency, while Powell’s model prediction agrees well with the experimental data. Note, however, if the constant κ is assumed to be 0.7, Powell’s model overpredicts the screech frequency compared with the experimental data, as shown by Tam (1988), while this model prediction would show good agreement with the experimental data. Whether this underprediction is due to an inaccurate κ is not yet clear and therefore requires further scrutiny. In figure 8(b), both of the two

Cases	κ	Λ	M_d	ν	N	N^*
1	0.8	2	1.5	1	4	3
2	0.73	2	1.5	2	4	3
3	0.64	2	1.5	3	4	3

TABLE 2. The operation conditions used in Gojon *et al.* (2019).

models provide favourable results. Specifically, Powell's model prediction agrees well with the experimental data when $M_i < 1.6$, while this model prediction agrees well with the experimental data at low Mach numbers and high Mach numbers. Generally speaking, the model prediction demonstrates favourable agreement with the experimental data (Raman & Rice 1994; Panda *et al.* 1997; Alkislar *et al.* 2003), suggesting that considering the additional phase delay may rectify the overprediction of the classical model.

In the final part of this section, we consider the thermal influence on the phase condition, which can be accounted for in two ways. Traditional model of the thermal effect is through the modification of U_c , as shown by (2.2). This effect was previously considered by Tam *et al.* (1986) for circular jet flow. They found that under different temperature ratios, the screech frequency can be predicted by

$$f = 0.67(M_i^2 - 1)^{-1/2} \left[1 + 0.7M_i \left(1 + \frac{\gamma - 1}{2} M_i^2 \right)^{-1/2} \nu^{1/2} \right]^{-1}. \quad (3.10)$$

In the rectangular jet flows, a similar formula may be obtained from (3.6) and (3.9), assuming $N = n$, $\Delta\phi = 0$, and $\kappa = 0.7$, i.e.

$$f = 0.35(M_i^2 - 1)^{-1/2} \left[1 + 0.7M_i \left(1 + \frac{\gamma - 1}{2} M_i^2 \right)^{-1/2} \nu^{1/2} \right]^{-1} \left[\left(\frac{1}{W} \right)^2 + 1 \right]^{\frac{1}{2}}. \quad (3.11)$$

Note that the difference between (3.10) and (3.11) arises from the distinct values of the shock spacing in circular and rectangular jet flows, which can be predicted by Pack's model (Pack 1950; Tam 1988), i.e. $s = \pi\sqrt{M_i^2 - 1}/2.4048$ for circular nozzles while $s = 2\sqrt{M_i^2 - 1}/\sqrt{1/W^2 + 1}$ for rectangular cases.

In this model, from figure 5, we can see that the phase delay is also changed by the temperature ratios. Therefore, to predict the screech frequency more accurately, the changes in the phase delay and the convection velocity U_c should be both accounted for. To quantitatively evaluate the thermal effects, we take three temperature ratios, i.e. $\nu = 1, 2$, and 3 into consideration. We calculate the transfer function at the screeching frequency under the three temperature ratios, the phase delays of which are shown in figure 9. Note that the screech frequency is calculated via (1.1) with the constant $\kappa = 0.7$. We can see that under the three temperature ratios phase delays increase as the jet Mach number increases. In addition, higher jet temperatures lead to larger phase delays ($\Delta\Phi_2$) across the entire range of Mach numbers, which will, according to (3.8), result in a lower

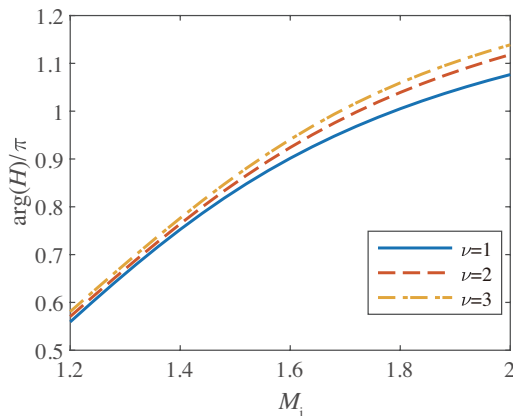


FIGURE 9. The phase delay between the upstream forcing and newly-excited instability wave at the screeching frequency. The parameter κ takes the value of 0.7 in the three cases and the angular frequency is calculated using (1.1).

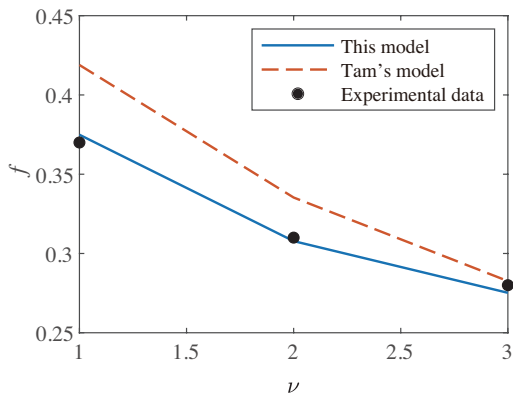


FIGURE 10. Comparison of Tam’s model prediction, this model prediction, and the experimental data (Gojon *et al.* 2019). The dashed red curve is calculated by Tam’s model. The solid blue line is obtained using this model. Filled circle points represent experimental data from Gojon *et al.* (2019).

frequency prediction. Note that this appears to contradict figure 5, but this apparent contradiction results from the fact that we are considering the phase delay at the screech frequency for each M_i and ν , whereas figure 5 considers the phase delay for a given M_i at the same frequency.

To quantitatively validate (3.8), we use the data from Gojon *et al.* (2019), where overexpanded jet flows under different temperature conditions were simulated using LES. The convection velocity of the instability waves was numerically obtained. They compared the frequency prediction from Tam’s model (Tam 1988) to the reported experimental results (Mora *et al.* 2016). “An overestimation of about 10%” (Gojon *et al.* 2019) compared to the experimental data was reported. This overprediction may be rectified if the calculated $\Delta\Phi_2$ is considered. To obtain the screech frequency prediction, we employ

the data of the convection velocity from Gojon *et al.* (2019) and evaluate (3.8) under the three different temperature ratios. The operation conditions are the same as those used in Gojon *et al.* (2019) and are listed in table 2. The comparison is shown in figure 10. These results indicate that if the additional phase delay is included, the predicted screech frequency agrees much better with the numerical simulation. Specifically, the overprediction from the classical model is rectified when the phase delay is considered.

4. Conclusion

This paper investigates the jet receptivity occurring at the nozzle lip within the screech feedback loop. The scattered field due to the upstream-propagating acoustic waves is derived using the Wiener-Hopf method, with the kernel decomposed through matched asymptotic expansions. To determine the newly-triggered instability wave, we impose the unsteady kutta condition by eliminating the emerging singularities in the scattered field. This results in a dispersion relation that governs the newly-excited instability waves. The transfer function between the newly-excited instability waves and the upstream forcing is subsequently obtained. The amplitude and phase of the transfer function are then discussed in detail.

The result shows that the scattering efficiency $|H|$ displays multiple peaks and valleys as the frequency increases. In addition, it is less than 5% under each operation condition that we consider. Moreover, the phase delay between the instability wave and the upstream forcing generally decreases as the frequency increases. Regarding the thermal influence on the transfer function, it is found that the scattering efficiency decreases slightly as the temperature ratio increases from 1 to 3, while higher jet temperatures can lead to lower phase delays at low frequencies but result in slightly higher phase delays at high frequencies.

Including this additional phase delay, we invoke the phase condition to predict the screech frequency. The new prediction demonstrates favourable agreement with the experimental data for cold supersonic jets. In particular, the overprediction of screech frequencies from classical models appears to be rectified using the present model, except for the case of Powell's measurement. In addition, we examine the effects of the temperature ratio on the screech frequency by including the additional phase delay, the result of which shows that the screech frequency prediction improves significantly.

Our future work would focus on the scattering efficiency obtained by the transfer function, which is not thoroughly investigated in this paper due to a lack of direct validation from experimental or numerical data in the open literature. Moreover, the frequency range under consideration is relatively small due to the requirement of the matched asymptotic expansions. We consider to use new strategies to overcome the limitations in our future study.

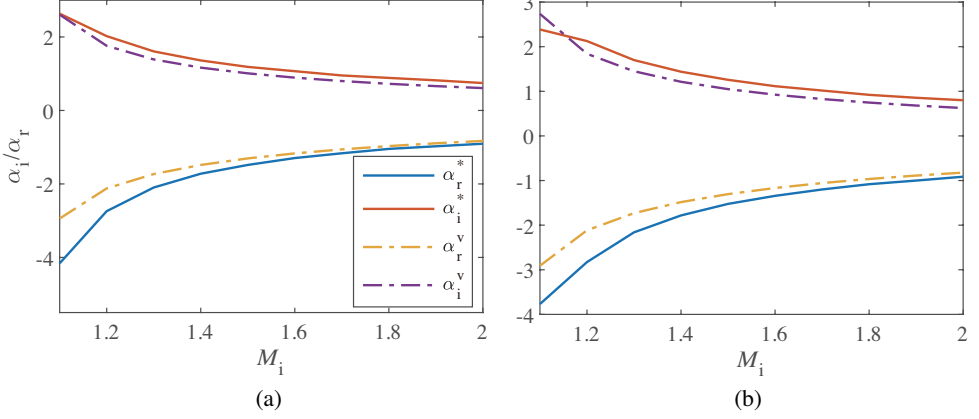


FIGURE 11. Comparison between the wavenumber numerically obtained by the dispersion relation and that calculated through the asymptotic expansions. The temperature ratio ν equals 3 and 5 in (a) and (b), respectively.

Appendix A.

Following the procedure of Ferrari's formula, zeros of the polynomial can be determined. Define a parameter y_a as

$$y_a = \sqrt[3]{c_2 + \sqrt{c_3}} + \sqrt[3]{c_2 - \sqrt{c_3}}, \quad (\text{A1})$$

where

$$c_2 = a_1^2/2, \quad (\text{A2})$$

$$c_3 = c_2^2 - 64a_0^3/27. \quad (\text{A3})$$

The zeros q_1, q_5, q_2, q_6 take the following forms, i.e.

$$q_{1,5} = -\frac{1}{2}\sqrt{y_a} \pm \frac{1}{2}\sqrt{-y_a + \frac{2a_1}{\sqrt{y_a}}}, \quad (\text{A4})$$

$$q_{2,6} = \frac{1}{2}\sqrt{y_a} \pm \frac{1}{2}\sqrt{-y_a - \frac{2a_1}{\sqrt{y_a}}}. \quad (\text{A5})$$

Zeros q_3, q_7, q_4, q_8 take similar forms, i.e.

$$q_{3,7} = -\frac{1}{2}\sqrt{y_a^*} \pm \frac{1}{2}\sqrt{-y_a^* - \frac{2a_1}{\sqrt{y_a^*}}}, \quad (\text{A6})$$

$$q_{4,8} = \frac{1}{2}\sqrt{y_a^*} \pm \frac{1}{2}\sqrt{-y_a^* + \frac{2a_1}{\sqrt{y_a^*}}}, \quad (\text{A7})$$

where

$$y_a^* = \sqrt[3]{c_2 + \sqrt{c_2^2 + c_3^*}} + \sqrt[3]{c_2 - \sqrt{c_2^2 + c_3^*}}, \quad (\text{A8})$$

$$c_3^* = c_2^2 - 64a_0^3/27. \quad (\text{A9})$$

It can be shown, by some algebra, that when the angular frequency $\omega > 0.05$ and $1 < M_i < 2$, $c_3 > 0$ and $c_3^* > 0$. In addition, y_a^* can be shown to be a real number.

With a negative real part and a positive imaginary part, $q_3 S^{4/3}$ (S is defined in section 2.2) corresponds to the wavenumber of the jet instability of the sinuous mode, which is defined as \mathcal{K} in (2.62). The original polynomial $R(q)$ has four zeros denoted as $q_{2,6}$ (in the right half-plane $\text{Re}(q) > 0$) and $q_{3,7}$ (in the left half-plane $\text{Re}(q) < 0$). The additional zeros are due to the increase in the polynomial order.

To further validate the decomposition, we present the additional comparison between the wavenumber numerically obtained by the dispersion relation and that calculated through the asymptotic expansions using different temperature ratios. We see that for the heated jets under consideration ($\nu = 3$ or $\nu = 5$) the agreement between the two wavenumbers remains satisfactory as $M_i > 1.2$.

Appendix B.

We first provide the detailed derivation from (2.50) to (2.51). Subtracting the left-hand side and right-hand side of (2.50) with $\sum_{n=1}^8 1/2(q - q_n)$, the left-hand side part can be directly written as

$$\frac{d}{dq} \ln \left(\frac{R_+(q)}{\prod_{n=5}^8 (q - q_n)^{1/2}} \right) + \frac{d}{dq} \ln \left(\frac{R_-(q)}{\prod_{n=1}^4 (q - q_n)^{1/2}} \right).$$

Using partial fraction decomposition, we can assume that the right-hand side part takes the following form, i.e.

$$\frac{(4q^3 + a_1|q|/q)(q^4 - a_1|q| + a_0)}{(q^4 + a_0)^2 - a_1^2 q^2} - \sum_{n=1}^8 \frac{1}{2(q - q_n)} = \sum_{n=1}^8 \xi_n \frac{1}{q - q_n} + \xi_9 \frac{1}{q - q_9}, \quad (\text{B1})$$

where $q_9 = 0$. The undetermined coefficient ξ_n can be calculated by multiplying the left-hand and right-hand side of (B1) with the corresponding $q - q_n$ and letting $q = q_n$ subsequently.

In what follows, we provide the detailed derivation from (2.51) to (2.57). Using the additive decomposition (2.54) and the identity (2.53), the right-hand side of (2.51) can be rewritten as

$$\sum_{n=1}^9 \xi_n \frac{q_n + \frac{iq_n}{\pi} \ln_+ q - \frac{iq_n}{\pi} \ln_- q}{q - q_n}, \quad (\text{B2})$$

which can be reorganized as

$$\sum_{n=1}^9 \xi_n \frac{\left(q_n + \frac{iq_n}{\pi} \ln_+ q_n - \frac{iq_n}{\pi} \ln_- - q_n \right) + \frac{iq_n}{\pi} \ln_+ q/q_n - \frac{iq_n}{\pi} \ln_- - q/q_n}{q - q_n}. \quad (\text{B3})$$

Using the identity (2.56), we can reduce (B 3) to

$$\sum_{n=1}^9 \xi_n \frac{\frac{iq_n}{\pi} \ln_+ q/q_n}{q - q_n} - \sum_{n=1}^9 \xi_n \frac{\frac{iq_n}{\pi} \ln_- q/q_n}{q - q_n} - \sum_{n=1}^9 \xi_n \frac{q_n}{q - q_n}.$$

Considering that $R_+(q)$ and $R_-(q)$ should be analytic and non-zero in the upper and lower half-planes respectively, we can properly write $R_+(q)$ as the form shown in (2.57).

Appendix C.

To calculate the acoustic wave propagating just outside the jet flow, i.e. $\phi_{\text{in}}(x, 1/2)$, it is convenient to deform the integration path in (2.3) along the branch cut of γ_1 at $k = \omega M_o$. In this way, the difference in the value of $D_o(\lambda)$ on two different sides of the branch cut only comes from γ_+ . $\phi_{\text{in}}(x, 1/2)$ can be thus expressed as

$$\phi_{\text{in}}(x, 1/2) = \frac{i}{2\pi} e^{-iM_o\omega x} \int_0^{+\infty} [D_o^*(M_o\omega + e^{i\pi/2}\zeta) - D_o^*(M_o\omega + e^{i3\pi/2}\zeta)] e^{\zeta x} d\zeta, \quad (\text{C1})$$

where $D^*(\zeta) = D_o(\zeta)/\exp(\gamma_+/2)$, and $\lambda = \omega M_o + i\zeta$. It is straightforward to see that only $\eta(\lambda)$ contains γ_+ (the definition of $\eta(\lambda)$ can be found in Li & Lyu (2023)). We can define a new function $E_o(\zeta)$ as follows:

$$E_o(\zeta) = D_o^*(\zeta)\eta(\zeta). \quad (\text{C2})$$

$\phi_{\text{in}}(x, 1/2)$ can be then reorganized as

$$\phi_{\text{in}}(x, 1/2) = \frac{-i}{\pi} e^{-iM_o\omega x} \int_0^{+\infty} E_o(\zeta) \frac{\omega^3 \coth(\gamma_-/2)\gamma_-}{\omega^4 \coth^2(\gamma_-/2)\gamma_-^2 - (\omega + \lambda)^4 \Delta^2(\zeta)} \frac{M_i^4}{M_o^4} e^{\zeta x} d\zeta, \quad (\text{C3})$$

where

$$\Delta(\zeta) = \sqrt{e^{\pi i/2}\zeta(i\zeta + 2M_o\omega)}. \quad (\text{C4})$$

Letting $\zeta^* = \zeta - iM_o\omega = -i\lambda$ and performing a coordinate transformation from $x = 0$ to $x = -h$, we can write the function $\mathcal{G}(\lambda)$ in (2.68) as

$$\mathcal{G}(\zeta^*) = \frac{-i}{\pi} E_o(\zeta^*) \frac{\omega^3 \coth(\gamma_-/2)\gamma_-}{\omega^4 \coth^2(\gamma_-/2)\gamma_-^2 - (\omega + \lambda)^4 \Delta^2(\zeta^*)} \frac{M_i^4}{M_o^4} e^{-\zeta^* h}. \quad (\text{C5})$$

It can be proved that as $\zeta^* \rightarrow 0$, $\mathcal{G}(\zeta^*)$ takes the following asymptotic forms, i.e.

$$\mathcal{G}(\zeta^*) = \mathcal{G}(0) + \mathcal{C}\zeta^* + O(\zeta^{*2}). \quad (\text{C6})$$

Here, $\mathcal{G}(0)$ is what we aim to find to determine ϵ in (2.70), which can be calculated by letting $\zeta^* = 0$ in (C5), while \mathcal{C} , a coefficient of order $O(1)$, is not presented here for clarity.

In what follows, we provide a proof of the relation (2.69), which is essential to uniquely determine ϵ . The approximated form of the upstream forcing can be written as

$$Ge^{\epsilon x}, \quad (\text{C7})$$

while without an approximation, the forcing reads

$$\int_0^\infty \mathcal{G}(\zeta^*) \exp(\zeta^* x) d\zeta^*. \quad (\text{C } 8)$$

These two expressions should be virtually the same when $x < 0$. Multiplying (C 7) and (C 8) with $e^{ikx}/K_+(k)$ and integrating each expression with respect to x from $-\infty$ to ∞ , we can find that (C 7) and (C 8) can be respectively evaluated as

$$\frac{2\pi G \delta(ik + \epsilon)}{K_+(k)} \quad \text{and} \quad \frac{2\pi \int_0^\infty \mathcal{G}(\zeta^*) \delta(ik + \zeta^*) d\zeta^*}{K_+(k)}. \quad (\text{C } 9)$$

Subsequently, integrating each expression with respect to k from $-\infty$ to ∞ yields (2.69).

Acknowledgments

The first author B. Li gratefully acknowledge Y. Ye for his helpful advice on numerical integration. The authors wish to gratefully acknowledge the financial support from Laoshan Laboratory under the grant number of LSKJ202202000.

REFERENCES

- ALAPATI, J. K. K. & SRINIVASAN, K. 2024 Screech receptivity control using exit lip surface roughness for under-expanded jet noise reduction. *Physica. Fluids* **36**(1), 016113.
- ALKISLAR, M. B., KROTHAPALLI, A. & LOURENCO, L. M. 2003 Structure of a screeching rectangular jet: a stereoscopic particle image velocimetry study. *J. Fluid Mech.* **489**, 121–154.
- BARONE, M. F. & LELE, S. K. 2005 Receptivity of the compressible mixing layer. *J. Fluid Mech.* **540**, 301–335.
- BATCHELOR, G. K. & GILL, A. E. 1962 Analysis of the stability of axisymmetric jets. *J. Fluid Mech.* **14**(4), 529–551.
- BERLAND, J., BOGEY, C. & BAILLY, C. 2007 Numerical study of screech generation in a planar supersonic jet. *Phys. Fluids* **19**(7), 075105.
- BOEGY, C. 2022 Interactions between upstream-propagating guided jet waves and shear-layer instability waves near the nozzle of subsonic and nearly ideally expanded supersonic free jets with laminar boundary layers. *J. Fluid Mech.* **949**, A41.
- BOGEY, C. 2023 Effects of nozzle-lip thickness on the tones in the near-field pressure spectra of high-speed jets. In *AIAA Aviation 2023 Forum. AIAA Paper 2023-3935*.
- CRIGHTON, D. G. 1972 The excess noise field of subsonic jets. *J. Fluid Mech.* **56**(4), 683–694.
- CRIGHTON, D. G. 1981 Acoustics as a branch of fluid mechanics. *J. Fluid Mech.* **106**, 261–298.
- CRIGHTON, D. G. 1985 The kutta condition in unsteady flow. *Annu. Rev. Fluid Mech.* **17**(1), 411–445.
- CRIGHTON, D. G. 1992 The jet edge-tone feedback cycle: linear theory for the operating stages. *J. Fluid Mech.* **234**, 361–391.
- CRIGHTON, D. G. 2001 Asymptotic factorization of wiener–hopf kernels. *Wave Motion* **33**(1), 51–65.
- EDGINGTON-MITCHELL, D. 2019 Aeroacoustic resonance and self-excitation in screeching and impinging supersonic jets – a review. *Int. J. Aeroacoust* **18**(2-3), 118–188.

- EDGINGTON-MITCHELL, D., JAUNET, V., JORDAN, P., TOWNE, A., SORIA, J. & HINNERY, D. 2018 Upstream-travelling acoustic jet modes as a closure mechanism for screech. *J. Fluid Mech.* **855**, R1.
- EDGINGTON-MITCHELL, D., LI, X., LIU, N., HE, F., WONG, T. Y., MACKENZIE, J. & NOGUEIRA, P. 2022 A unifying theory of jet screech. *J. Fluid Mech.* **945**, A8.
- EDGINGTON-MITCHELL, D., WANG, T., NOGUEIRA, P., SCHMIDT, O., JAUNET, V., DUKE, D., JORDAN, P. & TOWNE, A. 2021 Waves in screeching jets. *J. Fluid Mech.* **913**, A7.
- ERFELYI, A. 1958 *Asymptotic expansions*, 3rd edn., chap. 2. Cambridge: Pergamon.
- GOJON, R., BOGEY, C. & MIHAESCU, M. 2018 Oscillation modes in screeching jets. *AIAA J.* **56(7)**, 2918–2924.
- GOJON, R., GUTMARK, E. & MIHAESCU, M. 2019 Antisymmetric oscillation modes in rectangular screeching jets. *AIAA J.* **57(8)**, 3422–3441.
- GRADSHTEYN, I. S. & RYZHIK, I. M. 1980 *Table of Integrals, Series and Products.*, 3rd edn. Cambridge: Academic.
- HARPER-BOURNE, M. & FISHER, M. J. 1973 The noise from shock waves in supersonic jets. *AGARD Technical Report CP-131* **11**, 1–13.
- JORDAN, P., JAUNET, V., TOWNE, A., CAVALIERI, A. V. G., COLONIUS, T., SCHMIDT, O. & AGARWAL, A. 2018 Jet–flap interaction tones. *J. Fluid Mech.* **853**, 333–358.
- KAJI, S. & NISHIJIMA, N. 1996 Pressure field around a rectangular supersonic jet in screech. *AIAA J.* **34(10)**, 1990–1996.
- KARAMI, S. & SORIA, J. 2021 Influence of nozzle external geometry on wavepackets in under-expanded supersonic impinging jets. *J. Fluid Mech.* **929**, A20.
- KARAMI, S., STEGEMAN, P. C., OOI, A., THEOFILIS, V. & SORIA, J. 2020 Receptivity characteristics of under-expanded supersonic impinging jets. *J. Fluid Mech.* **889**, A27.
- KERSCHEN, E. J. 1996 Receptivity of shear layers to acoustic disturbances. In *1st AIAA Theoretical Fluid Mechanics Meeting*, *AIAA Paper 96-2135*.
- KROTHAPALLI, A., HSIA, Y., BAGANOFF, D. & KARAMECHETI, K. 1986 The role of screech tones in mixing of an underexpanded rectangular jet. *J. Sound Vib.* **106(1)**, 119–143.
- LI, B. & LYU, B. 2022 Acoustic emission due to the interaction between shock and instability waves in supersonic jet flow from a circular nozzle. In *28th AIAA/CEAS Aeroacoustics 2022 Conference*. *AIAA Paper 2022-3029*.
- LI, B. & LYU, B. 2023 Acoustic emission due to the interaction between shock and instability waves in two-dimensional supersonic jet flows. *J. Fluid Mech.* **954**, A35.
- LI, X., WU, X., LIU, L., ZHANG, X., HAO, P. & HE, F. 2023 Acoustic resonance mechanism for axisymmetric screech modes of underexpanded jets impinging on an inclined plate. *J. Fluid Mech.* **956**, A2.
- LI, X., ZHANG, X., HAO, P. & HE, F. 2020 Acoustic feedback loops for screech tones of underexpanded free round jets at different modes. *J. Fluid Mech.* **902**, 71–96.
- LI, X. D. & GAO, J. H. 2010 A multi-mode screech frequency prediction formula for circular supersonic jets. *J. Acoust. Soc. Am.* **127(3)**, 1251–1257.
- MALLA, B. & GUTMARK, E. 2017 Nearfield Characterization of a Low Supersonic Single Expansion Ramp Nozzle with Extended Ramps. In *55th AIAA Aerospace Sciences Meeting*. *AIAA Paper 2017-0131*.
- MANCINELLI, M., JAUNET, V., JORDAN, P. & TOWNE, A. 2021 A complex-valued resonance model for axisymmetric screech tones in supersonic jets. *J. Fluid Mech.* **928**, A32.

- MERCIER, B., CASTELAIN, T. & BAILLY, C. 2017 Experimental characterisation of the screech feedback loop in underexpanded round jets. *J. Fluid Mech.* **824**, 202–229.
- MERLE, M. 1956 Sur la fré'quencies des sondes e'mises par un jet d'air and 'a grand vitesse. *C. R. Academy of Science Paris* **243**, 490–493.
- MORA, P., BAIER, F., GUTMARK, E. J. & KAILASANATH, K. 2016 Acoustics from a Rectangular C-D Nozzle Exhausting over a Flat Surface. In *22nd AIAA/CEAS Aerospace Sciences Meeting and Exhibit. AIAA Paper 2016-1884*.
- MORATA, D. & PAMAMOSCHOU, D. 2023 Influence of nozzle external geometry on the emission of screech tones. *Int. J. Aeroacoust* **22(5-6)**, 459–480.
- NAGEL, R. T., DENHAM, J. W. & PAPANATHASIOU, A. G. 1983 Supersonic jet screech tone cancellation. *AIAA J.* **21**, 1541–1545.
- NOBLE, B. 1956 *Methods based on the Wiener-Hopf technique*, 3rd edn., p. 41. New York: Dover.
- NOGUEIRA, P. A. S., JAUNET, V., MANCINELLI, M., JORDAN, P. & EDGINGTON-MITCHELL, D. 2022 Closure mechanism of the a1 and a2 modes in jet screech. *J. Fluid Mech.* **936**, A10.
- NORUM, T. D. 1983 Screech suppression in supersonic jets. *AIAA J.* **21(2)**, 235–240.
- NORUM, T. D. 1984 Control of jet shock associated noise by a reflector. In *9th Aeroacoustics Conference, AIAA Paper 1984-2279*.
- PACK, D. C. 1950 A note on prandtl's formula for the wave-length of a supersonic gas jet. *Q. J. Journ. Mech. and Applied Math.* **3(2)**, 173–181.
- PANDA, J., RAMAN, G. & ZAMAN, K. B. M. Q. 1997 Underexpanded screeching jets from circular, rectangular and elliptic nozzles. In *22nd AIAA/CEAS Aerospace Sciences Meeting and Exhibit. AIAA Paper 97-1623*.
- PONTON, M. & SEINER, J. 1992 The effects of nozzle exit lip thickness on plume resonance. *J. Sound Vib.* **154(3)**, 531–549.
- POWELL, A. 1953a The noise of choked jets. *J. Acoust. Soc. Am.* **25(3)**, 385–389.
- POWELL, A. 1953b On the noise emanating from a two-dimensional jet above the critical pressure. *Aeronautical Quarterly* **4(2)**, 103–122.
- RAMAN, G. 1997 Screech tones from rectangular jets with spanwise oblique shock-cell structures. *J. Fluid Mech.* **330**, 141–168.
- RAMAN, G. 1999 Supersonic jet screech: Half-century from powell to the present. *J. Sound Vib.* **225(3)**, 543–571.
- RAMAN, G., PANDA, J. & ZAMAN, K. B. M. Q. 1997 Feedback and receptivity during jet screech: influence of an upstream reflector. In *3rd AIAA/CEAS Aeroacoustics Conference. AIAA Paper 97-0144*.
- RAMAN, G. & RICE, E. J. 1994 Instability modes excited by natural screech tones in a supersonic rectangular jet. *Phys. Fluids* **6(12)**, 3999–4008.
- SHEN, H. & TAM, C. K. W. 2000 Effects of jet temperature and nozzle-lip thickness on screech tones. *AIAA J.* **38(5)**, 762–767.
- STAVROPOULOS, M. N., MANCINELLI, M., JORDAN, P., JAUNET, V., WEIGHTMAN, J., EDGINGTON-MITCHELL, D. M. & NOGUEIRA, P. A. S. 2023 The axisymmetric screech tones of round twin jets examined via linear stability theory. *J. Fluid Mech.* **965**, A11.
- SUDA, H., MANNING, T. A. & KAJI, S. 1993 Transition of oscillation modes of rectangular supersonic jet in screech. In *15th AIAA Aeroacoustics Conference. AIAA Paper 93-4323*.
- TAM, C. K. W. 1972 On the noise of a nearly ideally expanded supersonic jet. *J. FLuid Mech.* **51**, 69–95.

- TAM, C. K. W. 1978 Excitation of instability waves in a two-dimensional shear layer by sound. *J. Fluid Mech.* **89(2)**, 357–371.
- TAM, C. K. W. 1986 On the screech tones of supersonic rectangular jets. In *10th Aeroacoustics Conference. AIAA Paper 86-1866*.
- TAM, C. K. W. 1988 The shock-cell structures and screech tone frequencies of rectangular and non-axisymmetric supersonic jets. *J. Sound Vib.* **121(1)**, 135–147.
- TAM, C. K. W. & REDDY, N. N. 1996 Prediction method for broadband shock-associated noise from supersonic rectangular jets. *J. Aircr.* **33(2)**, 298–303.
- TAM, C. K. W., SEINER, J. M. & YU, J. C. 1986 Proposed relationship between broadband shock associated noise and screech tones. *J. Sound Vib.* **110(2)**, 309–321.
- TAM, C. K. W., SHEN, H. & RAMAN, G. 1997 Screech tones of supersonic jets from bevelled rectangular nozzles. *AIAA J.* **35(7)**, 1119–1125.
- TAM, C. K. W. & TANNA, H. K. 1982 Shock associated noise of supersonic jets from convergent-divergent nozzles. *J. Sound Vib.* **81(3)**, 337–358.